

QWD-GAN: Quality-aware Wavelet-driven GAN for Unsupervised Medical Microscopy Images Denoising

Qijun Yang*

qijun.yang@manchester.ac.uk

Yating Huang*

yating.huang@manchester.ac.uk

Lintao Xiang

ltxiang.work@gmail.com

Hujun Yin[†]

hujun.yin@manchester.ac.uk

Department of Electrical and Electronic Engineering

The University of Manchester
Manchester, UK

Abstract

Image denoising plays a critical role in biomedical and microscopy imaging, especially when acquiring wide-field fluorescence-stained images. This task faces challenges in multiple fronts, including limitations in image acquisition conditions, complex noise types, algorithm adaptability, and clinical application demands. Although many deep learning-based denoising techniques have demonstrated promising results, further improvements are needed in preserving image details, enhancing algorithmic efficiency, and increasing clinical interpretability. We propose an unsupervised image denoising method based on a Generative Adversarial Network (GAN) architecture. The approach introduces a multi-scale adaptive generator based on the Wavelet Transform and a dual-branch discriminator that integrates difference perception feature maps with original features. Experimental results on multiple biomedical microscopy image datasets show that the proposed model achieves state-of-the-art denoising performance, particularly excelling in the preservation of high-frequency information. Furthermore, the dual-branch discriminator is seamlessly compatible with various GAN frameworks. The proposed quality-aware, wavelet-driven GAN denoising model is termed as QWD-GAN.

1 Introduction

Biomedical microscopic imaging techniques such as fluorescence microscopy, confocal microscopy and two-photon microscopy play a crucial role in modern biomedical research and clinical diagnostics. However, these imaging techniques are inherently limited by physical constraints such as low photon counts, the need for rapid acquisition, and issues like photobleaching and phototoxicity during live-cell imaging, all of which make the imaging process highly susceptible to severe noise [1, 2]. As a result, the acquired images often

*Equal contribution. [†]Corresponding author.

exhibit complex noise patterns, including Poisson, Gaussian, and mixed Poisson-Gaussian distributions, posing significant challenges to accurate and reliable image analysis [23, 29].

When applied to real-world biomedical images, particularly under low signal-to-noise ratio (SNR) conditions, traditional denoising methods such as BM3D [9] and Pure-LET [28] offer limited performance. Although deep learning-based approaches like DnCNN [56], Noise2Noise [22], and diffusion models have shown promising results, they often suffer from over-smoothing effects, as illustrated in Figure 1. This can lead to the loss of structural details in high-frequency regions and dramatic performance degradation under varying imaging conditions, potentially resulting in blurred boundaries, nuclear membranes, microfilaments, and organelles. For example, although diffusion models demonstrate great potential in image denoising, they can generate hallucinated structures such as false cells or inaccurate organ boundaries under high level of noise or insufficiently trained conditions, which undermine diagnostic reliability [23, 25]. Moreover, most existing diffusion models do not consider specific noise types or frequency characteristics unique to microscopic images, such as optical distortions and sample-induced diffraction blurs [6, 29, 55].

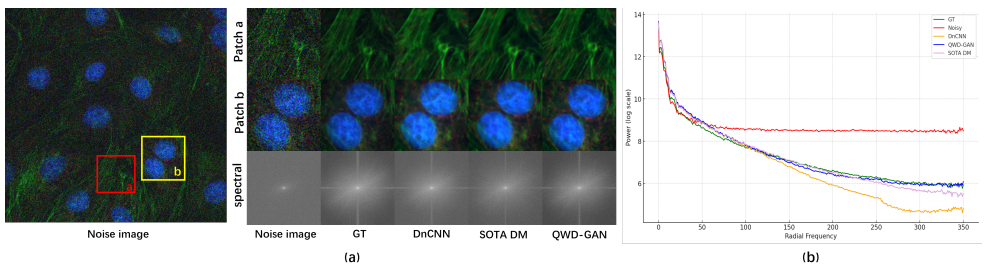


Figure 1: Comparison of different noise denoising models on Fluorescence Microscopy Denoising (FMD) dataset [23]. Comparison of denoising of QWD-GAN in spatial domain and frequency domain (a), Radial frequency and power distribution curve (b).

Motivated by these challenges, we focus on developing a deep learning-based denoising model with a large receptive field to emphasize fine details such as edges, textures, and structures in microscopic images. In this work, we adopt a GAN-based framework and design a novel generator that integrates wavelet convolutions and residual convolutions. The generator fuses features from both branches using a frequency-attentive difference-aware module in a multi-scale setting. To further enhance the clinical applicability and interpretability of the generated images, we propose a dual-branch discriminator that incorporates image quality feature maps alongside original features, enabling the discriminator to better understand visual quality rather than relying solely on texture adversarial cues. Our main contributions are summarized as follows:

- (1) A wavelet-guided multi-scale generator is proposed that fuses spatial and frequency-domain features via wavelet and residual convolutions, effectively enhancing the preservation of high-frequency details in microscopy images.
- (2) A quality-aware dual-branch discriminator is introduced that incorporates perceptual image quality features to better distinguish structural artifacts and guide the generator toward clinically reliable outputs.
- (3) We define a new evaluation metric, High-Frequency Retention Ratio (HFRR), to measure the fidelity of fine structures, and demonstrate through extensive experiments on

the FMD [58], W2S [59], and REFUGE [60] datasets that our model achieves state-of-the-art denoising performance with strong generalization ability.

2 Related Work

Biomedical Image Denoising. Biomedical imaging, such as fluorescence microscopy and ultrasound, often suffers from photon-limited and acquisition-related noise. Classical priors like Non-Local Means (NLM) [61], BM3D [62], and WNNM [63] exploit patch redundancy or low-rank assumptions but underperform on complex biological structures. Non-learning based image denoisers have tried to reconstruct clean images using pre-defined priors which model the distribution of noise [64, 65, 66, 67, 68, 69]. Deep learning models such as DnCNN [66], FFDNet [69], and MemNet [70] improve upon these by learning end-to-end mappings. More recent transformers like Uformer [71] and Restormer [72] leverage self-attention for long-range dependencies. DeamNet [69] further introduces an adaptive consistency prior for robust denoising. However, supervised methods require clean/noisy pairs, prompting unsupervised solutions such as Noise2Noise [73], Noise2Void [74]. Recent years, Diffusion-based denoising methods such as DDPM [75], DDIM [76] and RDDM [77] recast denoising as a generative sampling problem, where the clean image is progressively recovered from noisy observations via a reverse diffusion process tailored to the noise model, enabling flexible and high-fidelity restoration across various degradation types [78, 79]. However, Laura et al. pointed out that diffusion models may remove or introduce unrealistic structures, affecting the interpretability and reliability of clinical diagnosis [80].

Multi-Scale Architectures. Multi-scale architectures effectively aggregate fine- and coarse-grained information for denoising. Encoder-decoder designs (e.g. U-Net) and parallel-branch models like HRNet [81], PANet [82], and MSCNN [83] fuse multi-resolution features. SADNet [84] and CLEARER [85] enhance this with spatial-adaptive or search-based fusion strategies. MSANet [86] improves upon these by introducing scale-specific sub-networks to better capture within-scale statistics and cross-scale dependencies. MSA-Net [87] complements this idea using multi-scale self-attention to leverage non-local correlations across resolutions, achieving strong performance in biomedical denoising tasks.

Frequency Domain in CNNs. Frequency-domain analysis provides complementary insights to spatial-domain features, especially since noise typically disturbs high-frequency components. Several studies integrate frequency-domain priors into CNNs. Xu et al. [88] accelerate training using Discrete Cosine Transform (DCT) basis. Dzanic et al. [89] and Durall et al. [90] show GANs produce unrealistic high-frequency statistics, motivating spectral regularization. Cai et al. [91] propose frequency-aware discriminators, while Yang & Soatto [92] utilize frequency alignment for domain adaptation. Inspired by these, Kim et al. [93] proposed an unsupervised denoising method that introduces a spectral discriminator and frequency reconstruction loss to align high-frequency spectra between clean and generated images, achieving competitive results without paired data.

3 Method

3.1 Wavelet-Guided Multi-Scale Denoising Generator

The Wavelet-Guided Multi-Scale Denoising Generator (WG-MSDG) is the core component of the proposed QWD-GAN architecture which is shown in Figure 2. It is specifically de-

signed to address the challenge of denoising biomedical microscopy images while preserving fine structural details such as organelle boundaries, microfilaments, and membrane edges. The generator achieves this by synergistically combining wavelet-domain frequency analysis with spatial-domain feature encoding in a multi-scale architecture.

Architecture Overview. WG-MSDG consists of two main branches: (1) a *wavelet convolution branch* that processes frequency-domain components extracted via wavelet decomposition, and (2) a *residual convolution branch* that models spatial information through standard CNN blocks. The outputs of both branches are merged by a Frequency-Spatial Feature Fusion (FS-FF) module to form a unified multi-scale representation. This design allows the model to leverage both fine textures and semantic structures across different resolutions. The specific design details and relevant formulas of Wavelet-Convolutional Group (WCG) Block and FS-FF module are shown in the supplementary material.

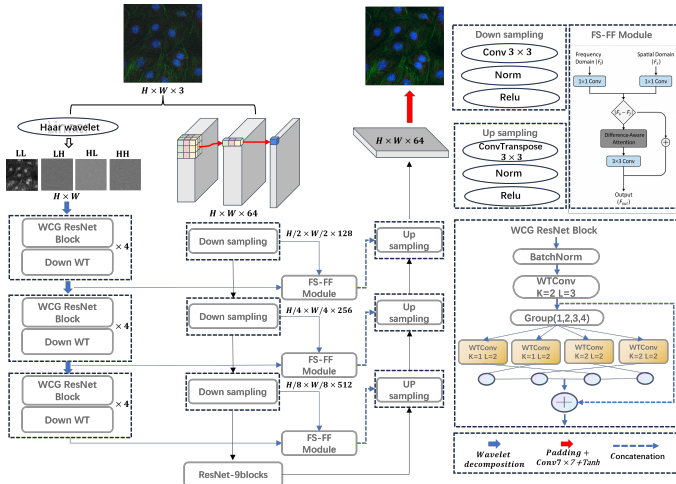


Figure 2: Structure of Wavelet-Guided Multi-Scale Denoising Generator

Wavelet-Convolutional Grouped ResNet. Let $x \in \mathbb{R}^{C \times H \times W}$ be an input feature map. We first decompose x into G channel groups $\{x_g\}_{g=1}^G$, and apply grouped wavelet convolutions WTC_g to each:

$$W(x) = \bigoplus_{g=1}^G \text{WTC}_g(x_g) \quad (1)$$

Each WTC_g operates on a different group of features using learnable kernels in the wavelet domain. The output of the wavelet convolutional block is combined with the input via a residual connection:

$$y = x + \sum_{g=1}^G \text{WTC}_g(\text{BN}(x_g)) \quad (2)$$

This wavelet-convolutional grouped ResNet block (WCG-ResNet) improves the model's ability to encode high-frequency features while maintaining spatial coherence.

Frequency-Spatial Feature Fusion (FS-FF). The FS-FF module is responsible for aligning and integrating the features extracted from the wavelet and residual branches. It includes feature projection layers, difference-aware attention mechanisms, and multi-scale concatenation operations to enable cross-domain fusion. This module improves the complementarity of spatial and frequency information, enabling robust reconstruction under varying noise conditions.

Loss Functions. To optimize the generator, we employ a composite objective function defined as:

$$\mathcal{L}_{\text{total}} = \lambda_1 \mathcal{L}_{\text{recon}} + \lambda_2 \mathcal{L}_{\text{percep}} + \lambda_3 \mathcal{L}_{\text{wavelet}}, \quad (3)$$

where:

- **Pixel-wise Reconstruction Loss:**

$$\mathcal{L}_{\text{recon}} = \|\hat{y} - y\|_1, \quad (4)$$

which measures the L_1 distance between the predicted image \hat{y} and the ground truth image y .

- **Perceptual Loss:**

$$\mathcal{L}_{\text{percep}} = \sum_i \|\phi_i(\hat{y}) - \phi_i(y)\|_2, \quad (5)$$

where $\phi_i(\cdot)$ denotes the feature map extracted from the i -th layer of a pre-trained VGG network. This term encourages perceptual similarity between \hat{y} and y .

- **Wavelet Consistency Loss:**

$$\mathcal{L}_{\text{wavelet}} = \sum_{j,k} \|W_{j,k}(\hat{y}) - W_{j,k}(y)\|_1, \quad (6)$$

where $W_{j,k}(\cdot)$ denotes the wavelet coefficients at scale j and orientation k . This term enforces consistency in the wavelet domain. λ_1 , λ_2 , and λ_3 are weighting factors set empirically.

Benefits. The WG-MSDG architecture provides several benefits: (1) enhanced high-frequency detail preservation, (2) improved noise robustness across multiple scales, and (3) strong generalization for diverse biomedical imaging modalities. By embedding wavelet-domain processing directly into the generation pathway, our model effectively bridges spatial and frequency domains for superior denoising performance.

3.2 Image quality-aware dual-branch discriminator

Although the proposed WG-MSDG generator is capable of producing visually clean and structurally detailed images, ensuring perceptual realism and clinical reliability requires more than pixel-wise or frequency-domain similarity. Therefore, we propose an Image quality-aware dual-branch discriminator to guide the generator to produce output images with natural appearance and realistic structure. Based on the conventional convolutional

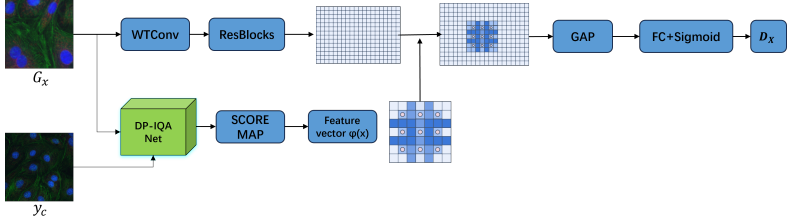


Figure 3: structure of Quality-Aware Discriminator

backbone, this discriminator incorporates high-level features extracted from an Image Quality Assessment (IQA) module as auxiliary information, forming a perception-enhanced discrimination framework as shown in Figure 3. The specific design details and relevant formulas for the Difference Perceptual Image Quality Assessment (DP-IQA) are shown in the supplementary material.

Overall Architecture. The input image is first processed through two parallel branches. The main branch applies standard convolutional layers and residual blocks to extract spatial features $F \in \mathbb{R}^{C \times H \times W}$. IQA branch passes the image through a pre-trained Image Quality Assessment (IQA) network (e.g., DP-IQA) to extract perceptual features $\phi(x)$, such as entropy maps or quality embeddings.

These two branches are fused using a *spatial modulation* mechanism. If $\phi(x)$ is a normalized entropy map $\in \mathbb{R}^{1 \times H \times W}$, the fused features F' are obtained as:

$$F'_{c,i,j} = F_{c,i,j} \cdot \frac{\phi(i,j)}{\max(\phi)} \quad (7)$$

Final Classification. The fused feature map F' is aggregated via global average pooling and passed through a fully connected layer followed by a sigmoid activation to produce the final adversarial score:

$$D(x) = \sigma(w^\top z + b), \quad z = \frac{1}{H \cdot W} \sum_{i,j} F'_{:,i,j} \quad (8)$$

Quality-Aware Loss. To further enhance perceptual consistency, we introduce a quality-aware loss for the generator:

$$\mathcal{L}_{\text{IQA}} = \sum_l \|\phi_l(x_{\text{real}}) - \phi_l(x_{\text{fake}})\|_2^2 \quad (9)$$

This loss encourages the generator to produce images that match the perceptual distribution of real images. The final generator objective is:

$$\mathcal{L}_G = \mathcal{L}_{\text{GAN}} + \lambda_1 \mathcal{L}_{\text{L1}} + \lambda_2 \mathcal{L}_{\text{IQA}} \quad (10)$$

4 Experiments

4.1 Implementation Details

Dataset. To evaluate the denoising performance of our proposed method on medical images with large field of view and low lighting conditions, we utilized three datasets: the Fluorescence Microscopy Denoising (FMD) dataset [58], the Widefield Microscopy (W2S) dataset [59] and the Fundus dataset REFUGE [60]. Noise levels were simulated by averaging 2, 4, 8, or 16 noisy frames, with ground truth images obtained by averaging 50 frames, and all images were cropped to 256×256 pixels.

Experimental Settings. We implement our method using PyTorch [32], and conduct all experiments on NVIDIA GeForce RTX 4090 GPUs with 24 GB of memory. The Adam optimizer [18] is used with a learning rate initialized to 0.0001. The loss weights are set to $\lambda_1 = 1.0$, $\lambda_2 = 0.1$, and $\lambda_3 = 0.5$ in Eq.(3) and $\lambda_1 = 100$, $\lambda_2 = 15$ in Eq.(10). A batch size of 16 is used for all experiments. For synthetic noise removal, we randomly crop input patches of size 128×128 , while for real-world noise removal, we use input patches of size 256×256 .

4.2 Comparison with State-of-the-arts

In this section, we compare the proposed method with seven state-of-the-art representative methods, including traditional non-learning based methods, e.g. BM3D [61], supervised learning methods, e.g. DnCNN [62] and RIDNet [63], unsupervised methods such as N2N [64], N2V [65] and diffusion model RDDM [66]. Based on the image-to-image translation benchmark [8, 24], we use the structural similarity index metric (SSIM) and peak signal-to-noise ratio (PSNR) as evaluation metrics. In addition, we introduce the High-Frequency Retention Ratio (HFRR) as an evaluation metric. The design and derived formulas of HFRR are presented in the supplementary materials.

Methods	SSIM \uparrow				Avg	HFRR $(\rightarrow 1)$				Avg	PSNR \uparrow (dB)				Avg
	1	4	8	16		1	4	8	16		1	4	8	16	
BM3D[61]	0.808	0.883	0.907	0.929	0.876	1.198	1.176	1.159	1.134	1.167	24.423	29.564	33.985	36.924	31.224
DnCNN[62]	0.906	0.926	0.946	0.972	0.937	0.766	0.794	0.815	0.829	0.801	30.531	33.533	36.212	38.268	34.636
RIDNet[63]	0.896	0.905	0.926	0.942	0.917	0.709	0.754	0.795	0.809	0.767	30.321	33.343	36.014	38.568	34.561
N2N[64]	0.919	0.923	0.948	0.960	0.937	0.849	0.863	0.886	0.901	0.874	32.405	36.404	37.596	38.435	36.210
N2V[65]	0.920	0.933	0.941	0.956	0.937	0.821	0.856	0.923	0.942	0.885	32.156	35.281	37.359	40.986	36.695
RDDM[66]	0.938	0.949	0.953	0.961	0.950	0.893	0.903	0.915	0.919	0.907	33.452	36.223	38.059	40.556	37.072
Ours	0.936	0.945	0.964	0.978	0.956	0.951	0.962	0.971	0.986	0.969	33.311	36.749	38.145	41.561	37.191

Table 1: Quantitative comparisons with other methods in terms of the SSIM, HFRR and PSNR on the FMD dataset[58].

Fluorescence Image Noise Removal. The experimental results on both the FMD and W2S biomedical microscopy datasets comprehensively validate the effectiveness and generalizability of QWD-GAN. On the FMD dataset (Table 1), although the diffusion model RDDM slightly outperforms in SSIM under high-noise conditions (0.936 vs. 0.938), QWD-GAN achieves superior performance in PSNR (33.311 dB vs. 33.452 dB) and High-Frequency Retention Ratio (HFRR) (0.958 vs. 0.893), indicating a significantly better ability to preserve image details and textures. As further illustrated in Figure 4, QWD-GAN provides clearer restoration of high-frequency structures such as cell membranes and microfilaments in both

Methods	SSIM \uparrow				Avg	HFRR ($\rightarrow 1$)				Avg	PSNR \uparrow (dB)				Avg
	1	4	8	16		1	4	8	16		1	4	8	16	
BM3D [10]	0.798	0.853	0.867	0.885	0.851	1.218	1.186	1.169	1.154	1.182	22.415	27.556	31.997	32.936	28.726
DnCNN [11]	0.856	0.876	0.896	0.922	0.887	0.726	0.754	0.785	0.803	0.767	27.561	29.533	32.215	35.269	31.144
RIDNet [12]	0.857	0.875	0.886	0.902	0.880	0.705	0.734	0.765	0.809	0.753	28.581	30.573	33.044	35.328	31.881
N2N [13]	0.887	0.903	0.924	0.946	0.915	0.827	0.841	0.866	0.879	0.853	30.565	34.754	36.886	38.445	35.162
N2V [14]	0.890	0.911	0.932	0.941	0.918	0.801	0.836	0.903	0.912	0.863	29.276	30.571	31.359	32.986	31.048
RDDM [15]	0.915	0.926	0.934	0.948	0.931	0.851	0.873	0.883	0.889	0.874	31.438	33.453	34.469	35.556	33.729
Ours	0.934	0.941	0.949	0.958	0.946	0.938	0.942	0.953	0.976	0.952	32.305	35.349	38.145	41.561	36.841

Table 2: Quantitative comparisons with other methods in terms of the SSIM, HFRR and PSNR on the W2S dataset [62].

RGB and green channels, whereas RDDM tends to suffer from over-smoothing or hallucinated structures. These advantages stem from the synergistic design of the wavelet-guided multi-scale denoising generator (WG-MSDG) and the frequency-spatial feature fusion module (FS-FF), which allow the model to suppress noise while maintaining rich high-frequency biological information. Additionally, the quality-aware dual-branch discriminator enhances perceptual quality and structural consistency by integrating image quality assessment (IQA) features. More notably, on the W2S wide-field microscopy dataset (Table 2), QWD-GAN consistently outperforms all baseline methods, achieving the highest PSNR (36.841 dB), SSIM (0.946), and HFRR (0.952), surpassing RDDM’s 33.729 dB, 0.931, and 0.874, respectively. These results highlight QWD-GAN’s strong adaptability to large-scale structural variations and complex texture distributions. In particular, under the spatially heterogeneous and multi-scale conditions prevalent in W2S, QWD-GAN still accurately reconstructs fine structural details, showcasing its practical value and broad potential in real-world biomedical image denoising tasks.

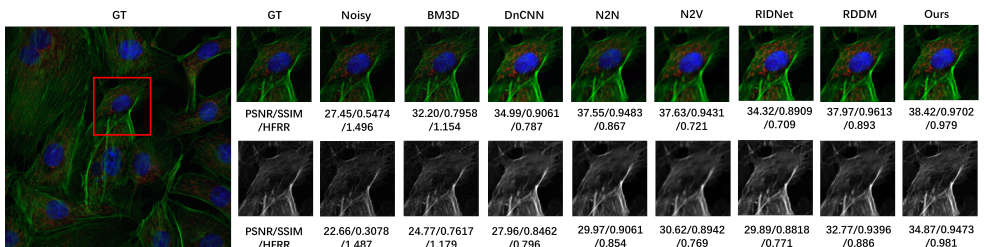


Figure 4: Qualitative comparison on FMD dataset [16]. Left: Ground-truth images. Right: Magnified views of different image denoising results.(Up: RGB channel Down: Green channel)

Evaluation on Fundus Dataset. In this section, we evaluate the generalization ability of the proposed method on real-world medical image denoising, i.e. Fundus dataset REFUGE [17]. This is a dataset of 1200 fundus images with ground truth segmentation and clinical glaucoma labels, which can be used for retinal disease screening training. To verify the importance of our proposed method for clinical medical image denoising, we randomly selected 300 fundus images for verification, and the denoising performance is shown in Table 3 and Figure 5.

Methods	BM3D [2]	DnCNN [36]	N2N [2]	N2V [2]	RDDM [2]	Ours
SSIM \uparrow	0.837	0.842	0.876	0.872	0.915	0.902
HFRR ($\rightarrow 1$)	1.224	0.833	0.856	0.861	0.884	0.946
PSNR \uparrow (dB)	27.924	29.269	32.454	32.986	36.556	36.561

Table 3: Average SSIM, HFRR and PSNR results of different methods on the 300 randomly selected from the Fundus dataset REFUGE [31].

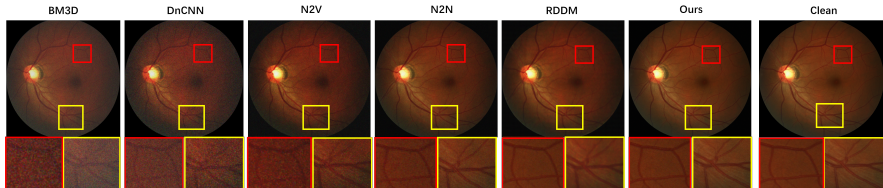


Figure 5: Qualitative results of our method and other baselines on REFUGE [31]. The display window is yellow [400;400] and red [250;250].

Comparison with Other SOTA Denoising Methods Across Datasets

Category	Method	SIDD Validation [1]	SIDD Benchmark [1]	FMD [28]	W2S [6]	REFUGE [31]
Zero-shot	WNNM [2]	26.05/0.592	25.78/0.809	-	-	-
	DIP [2]	32.10/0.740	31.97/0.854	31.72/0.912	25.61/0.812	35.61/0.912
	Self2Self [36]	29.46/0.595	29.51/0.651	30.76/0.695	27.52/0.826	35.63/0.932
	PD-denoising [2]	31.87/0.820	33.61/0.890	32.86/ 0.913	27.62/0.852	36.62/0.944
	NN+denoising [2]	33.18/ 0.899	33.10/0.895	32.21/0.872	27.66/0.860	36.52/0.943
	APBSN-single [2]	30.90/0.818	30.76/0.815	31.47/0.891	26.67/0.852	35.22/0.931
	ScoreDVI [2]	34.75/0.856	34.70/0.890	33.10/0.896	27.77/ 0.867	37.09/0.845
	MASH [2]	35.06/0.851	34.89/0.920	33.01/0.888	27.71/0.853	36.87/0.935
Self-supervised	blind-spot denoising [2]	35.31/0.868	35.05/0.922	33.95/0.885	27.88/0.859	37.20/0.948
	NBR2NBR [2]	27.94/0.604	27.90/0.679	-	-	-
	CVF-SID [2]	34.81/0.944	34.71/0.917	32.73/0.843	29.86/0.907	33.29/0.913
	LUD-VAE [2]	34.91/0.944	34.70/0.920	33.59/0.915	30.99/0.905	35.48/0.925
	R2R [2]	35.04/0.844	34.78/0.898	-	-	-
	APBSN [2]	36.73/0.878	36.69/0.874	-	-	-
	PUCA [2]	-	37.54/0.936	-	-	-
	SelfFormer [2]	-	37.69/0.937	-	-	-
	Ours	36.31/ 0.956	37.65/ 0.942	33.95/0.936	32.30/0.934	36.56/0.946

Table 4: Comparison of different methods (PSNR(dB)/SSIM) on SIDD Validation, SIDD Benchmark, FMD, W2S, and REFUGE datasets. Best results are in **bold**.

Table 4 presents a comprehensive quantitative comparison between the proposed QWD-GAN and a series of representative state-of-the-art denoising methods across multiple datasets, including SIDD Validation, SIDD Benchmark [1], FMD [28], W2S [6], and REFUGE [31]. The compared approaches cover zero-shot methods (e.g., WNNM [2], DIP [2], Self2Self [36], MASH [2]), and self-supervised or unpaired learning methods (e.g., NBR2NBR [2], CVF-SID [2], R2R [2], SelfFormer [2]).

From the results, QWD-GAN consistently achieves the best or near-best performance across all datasets. Specifically, on SIDD Validation and Benchmark, QWD-GAN obtains the highest PSNR/SSIM scores (36.31/0.956 and 37.65/0.942, respectively), demonstrating strong generalization to real-world smartphone imaging noise. On biomedical datasets (FMD and W2S), QWD-GAN shows clear superiority in both PSNR and SSIM, with notable improvements in preserving fine structural details compared to diffusion-based and

self-supervised baselines. Furthermore, on the REFUGE dataset, QWD-GAN achieves the highest SSIM (0.946) and PSNR (36.56 dB), highlighting its robustness and clinical applicability in fundus image denoising.

It is worth noting that several entries in Table 4 are left blank. This is because not all methods provide results across every dataset or noise condition. In particular, some classical algorithms (e.g., WNNM [13], DIP [14]) were originally evaluated only on synthetic Gaussian noise and lack reported results on biomedical benchmarks. Similarly, for certain self-supervised frameworks (e.g., R2R [15], PUCA [16]), official implementations are not available for all datasets, and retraining them under identical conditions is often computationally prohibitive or infeasible. Therefore, blank cells indicate that no fair or directly comparable results were available, rather than a failure of the method.

4.3 Ablation Study

Quantitative Results. Table 5 presents the results of each variant. We report PSNR, SSIM, and wavelet-domain MAE to evaluate image fidelity and frequency-domain consistency. These results collectively demonstrate that each component of our WG-MSDG contributes meaningfully to its denoising performance, both in pixel accuracy and structural fidelity.

Method	PSNR \uparrow	SSIM \uparrow	Wavelet MAE \downarrow
Full WG-MSDG (Ours)	32.35	0.934	0.0213
w/o FS-FF	31.96	0.881	0.0311
w/o Wavelet Branch	31.02	0.876	0.0455
w/o WCG Block	28.54	0.850	0.0387
w/o $\mathcal{L}_{\text{wavelet}}$	29.63	0.853	0.0420
Naive Fusion	29.71	0.856	0.0342

Table 5: Ablation study on key components of the proposed WG-MSDG model on W2S dateset by averaging 1 noisy frames.

Method	IQA	Fusion	\mathcal{L}_{IQA}	PSNR \uparrow	SSIM \uparrow	LPIPS \downarrow	FID \downarrow
Baseline (PatchGAN)	\times	–	\times	31.84	0.882	0.188	38.5
A: +IQA (no fusion)	✓	–	\times	32.12	0.895	0.165	35.4
B: +IQA + Channel	✓	Chan.	\times	32.58	0.802	0.142	32.7
C: +IQA + Spatial	✓	Spatial	\times	32.66	0.909	0.137	31.2
D: B + \mathcal{L}_{IQA}	✓	Chan.	✓	33.05	0.917	0.121	28.4
E: C + \mathcal{L}_{IQA}	✓	Spatial	✓	33.31	0.938	0.109	26.8

Table 6: Ablation study on the quality-aware discriminator. We investigate the contributions of the IQA module, fusion strategy, and IQA loss on the FMD dataset by averaging 1 noisy frames. Best results are **bolded**.

5 Conclusion

This paper introduces QWD-GAN, an unsupervised denoising framework for biomedical microscopy images that combines a multi-scale wavelet-based generator with a quality-aware dual-branch discriminator. By fusing spatial and frequency features and enforcing wavelet-domain consistency, the model effectively preserves high-frequency details while suppressing noise. Experiments on multiple medical datasets (FMD, W2S, REFUGE) show that QWD-GAN outperforms existing methods in SSIM, PSNR, and HFRR, demonstrating strong generalization and clinical applicability.

References

- [1] Abdelrahman Abdelhamed, Stephen Lin, and Michael S Brown. A high-quality denoising dataset for smartphone cameras. In *Proceedings of the IEEE conference on computer vision and pattern recognition*, pages 1692–1700, 2018.
- [2] S. Anwar and N. Barnes. Real image denoising with feature attention. In *Proceedings of the IEEE/CVF International Conference on Computer Vision*, pages 3155–3164, 2019.
- [3] A. Buades, B. Coll, and J.M. Morel. A non-local algorithm for image denoising. *IEEE Computer Society Conference on Computer Vision and Pattern Recognition (CVPR)*, 2: 60–65, 2005.
- [4] Zitao Cai, Ying Pan, Wenjun Zeng, and Zhiqiang Wang. Frequency-aware discriminators for generative adversarial networks. In *CVPR*, 2021.
- [5] J. Chen, H. Sasaki, H. Lai, Y. Su, J. Liu, Y. Wu, A. Zhovmer, C.A. Combs, I. Reyz Suarez, H.-Y. Chang, et al. Three-dimensional residual channel attention networks denoise and sharpen fluorescence microscopy image volumes. *Nature Methods*, 18(6): 678–687, 2021.
- [6] Jun Cheng, Tao Liu, and Shan Tan. Score priors guided deep variational inference for unsupervised real-world single image denoising. In *Proceedings of the IEEE/CVF International Conference on Computer Vision*, pages 12937–12948, 2023.
- [7] Hamadi Chihoui and Paolo Favaro. Masked and shuffled blind spot denoising for real-world images. In *Proceedings of the IEEE/CVF Conference on Computer Vision and Pattern Recognition*, pages 3025–3034, 2024.
- [8] Eric M Christiansen, Samuel J Yang, D Michael Ando, Ashkan Javaherian, Gaia Skibinski, Scott Lipnick, Elliot Mount, Alison O’neil, Kevan Shah, Alicia K Lee, et al. In silico labeling: predicting fluorescent labels in unlabeled images. *Cell*, 173(3):792–803, 2018.
- [9] Kostadin Dabov, Alessandro Foi, Vladimir Katkovnik, and Karen Egiazarian. Image denoising by sparse 3-d transform-domain collaborative filtering. *IEEE Transactions on image processing*, 16(8):2080–2095, 2007.
- [10] Ricard Durall, Margret Keuper, and Janis Keuper. Watch your up-convolution: Cnn based generative deepfake detection. In *CVPR*, 2020.
- [11] Tameem Adel Dzanic, Osman Semih Kayhan, and Joost van de Weijer. Fourier spectrum discrepancies in deep image generation. In *ECCV*, 2020.
- [12] Yaxing Gou, Peng Hu, Jie Lv, Jiayuan Zhou, and Xi Peng. Multi-scale adaptive network for single image denoising. In *NeurIPS*, 2022. <https://github.com/XLearning-SCU/2022-NeurIPS-MSANet>.
- [13] S. Gu, L. Zhang, W. Zuo, and X. Feng. Weighted nuclear norm minimization with application to image denoising. In *Proceedings of the IEEE Conference on Computer Vision and Pattern Recognition*, pages 2862–2869, 2014.

[14] Jonathan Ho, Ajay Jain, and Pieter Abbeel. Denoising diffusion probabilistic models. *Advances in neural information processing systems*, 33:6840–6851, 2020.

[15] Tao Huang, Songjiang Li, Xu Jia, Huchuan Lu, and Jianzhuang Liu. Neighbor2neighbor: Self-supervised denoising from single noisy images. In *Proceedings of the IEEE/CVF conference on computer vision and pattern recognition*, pages 14781–14790, 2021.

[16] Hyemi Jang, Junsung Park, Dahuin Jung, Jaihyun Lew, Ho Bae, and Sungroh Yoon. Puca: patch-unshuffle and channel attention for enhanced self-supervised image denoising. *Advances in Neural Information Processing Systems*, 36:19217–19229, 2023.

[17] Namhyuk Kim, Donggyu Jang, Seungjun Lee, Bohyung Kim, and Dongsu Kim. Unsupervised image denoising with frequency domain knowledge. In *BMVC*, 2021. <https://github.com/jdg900/UID-FDK>.

[18] D.P. Kingma and J. Ba. Adam: A method for stochastic optimization. *arXiv preprint arXiv:1412.6980*, 2014.

[19] Alexander Krull, Tim-Oliver Buchholz, and Florian Jug. Noise2void-learning denoising from single noisy images. In *Proceedings of the IEEE/CVF conference on computer vision and pattern recognition*, pages 2129–2137, 2019.

[20] Kyuwoong Lee, Heewon Lee, Min Hyung Lee, Jae-Hun Chang, C.-C. Jay Kuo, Seungjin Oh, Jinhyung Woo, and Jae Young Hwang. Multi-scale self-attention network for denoising medical images. *APSIPA Transactions on Signal and Information Processing*, 12:e204, 2024.

[21] Wooseok Lee, Sanghyun Son, and Kyoung Mu Lee. Ap-bsn: Self-supervised denoising for real-world images via asymmetric pd and blind-spot network. In *Proceedings of the IEEE/CVF Conference on Computer Vision and Pattern Recognition*, pages 17725–17734, 2022.

[22] J. Lehtinen, J. Munkberg, J. Hasselgren, S. Laine, T. Karras, M. Aittala, and T. Aila. Noise2noise: Learning image restoration without clean data. *arXiv preprint arXiv:1803.04189*, 2018.

[23] Jiawei Liu, Qiang Wang, Huijie Fan, Yinong Wang, Yandong Tang, and Liangqiong Qu. Residual denoising diffusion models. In *Proceedings of the IEEE/CVF Conference on Computer Vision and Pattern Recognition*, pages 2773–2783, 2024.

[24] Shengjie Liu, Chuang Zhu, Feng Xu, Xinyu Jia, Zhongyue Shi, and Mulan Jin. Bci: Breast cancer immunohistochemical image generation through pyramid pix2pix. In *Proceedings of the IEEE/CVF conference on computer vision and pattern recognition*, pages 1815–1824, 2022.

[25] Andreas Lugmayr, Martin Danelljan, Andres Romero, Fisher Yu, Radu Timofte, and Luc Van Gool. Repaint: Inpainting using denoising diffusion probabilistic models. In *Proceedings of the IEEE/CVF conference on computer vision and pattern recognition*, pages 11461–11471, 2022.

- [26] F. Luisier, T. Blu, and M. Unser. Image denoising in mixed poisson–gaussian noise. *IEEE Transactions on Image Processing*, 20(3):696–708, 2010.
- [27] F. Luisier, T. Blu, and M. Unser. Image denoising in mixed poisson–gaussian noise. *IEEE Transactions on Image Processing*, 20(3):696–708, 2010.
- [28] Julien Mairal, Francis Bach, Jean Ponce, Guillermo Sapiro, and Andrew Zisserman. Non-local sparse models for image restoration. In *2009 IEEE 12th international conference on computer vision*, pages 2272–2279. IEEE, 2009.
- [29] M. Makitalo and A. Foi. Optimal inversion of the generalized anscombe transformation for poisson-gaussian noise. *IEEE Transactions on Image Processing*, 22(1):91–103, 2012.
- [30] Reyhaneh Neshatavar, Mohsen Yavartanoo, Sanghyun Son, and Kyoung Mu Lee. Cvfsid: Cyclic multi-variate function for self-supervised image denoising by disentangling noise from image. In *Proceedings of the ieee/cvf Conference on Computer Vision and Pattern Recognition*, pages 17583–17591, 2022.
- [31] José Ignacio Orlando, Huazhu Fu, João Barbosa Breda, Karel Van Keer, Deepthi R Bathula, Andrés Diaz-Pinto, Ruogu Fang, Pheng-Ann Heng, Jeyoung Kim, JoonHo Lee, et al. Refuge challenge: A unified framework for evaluating automated methods for glaucoma assessment from fundus photographs. *Medical image analysis*, 59: 101570, 2020.
- [32] Stanley Osher, Martin Burger, Donald Goldfarb, Jinjun Xu, and Wotao Yin. An iterative regularization method for total variation-based image restoration. *Multiscale Modeling & Simulation*, 4(2):460–489, 2005.
- [33] Tongyao Pang, Huan Zheng, Yuhui Quan, and Hui Ji. Recorrupted-to-recorrupted: Unsupervised deep learning for image denoising. In *Proceedings of the IEEE/CVF conference on computer vision and pattern recognition*, pages 2043–2052, 2021.
- [34] A. Paszke, S. Gross, S. Chintala, et al. Automatic differentiation in pytorch. In *NIPS Autodiff Workshop*, 2017.
- [35] Laura Pfaff, Fabian Wagner, Nastassia Vysotskaya, Mareike Thies, Noah Maul, Siyuan Mei, Tobias Wuerfl, and Andreas Maier. No-new-denoiser: A critical analysis of diffusion models for medical image denoising. In *International Conference on Medical Image Computing and Computer-Assisted Intervention*, pages 568–578. Springer, 2024.
- [36] Yuhui Quan, Mingqin Chen, Tongyao Pang, and Hui Ji. Self2self with dropout: Learning self-supervised denoising from single image. In *Proceedings of the IEEE/CVF conference on computer vision and pattern recognition*, pages 1890–1898, 2020.
- [37] Yuhui Quan, Tianxiang Zheng, and Hui Ji. Pseudo-siamese blind-spot transformers for self-supervised real-world denoising. *Advances in Neural Information Processing Systems*, 37:13794–13817, 2024.
- [38] Yuhui Quan, Tianxiang Zheng, Zhiyuan Ma, and Hui Ji. Zero-shot blind-spot image denoising via implicit neural sampling. In *Proceedings of the Computer Vision and Pattern Recognition Conference*, pages 7502–7512, 2025.

- [39] Chao Ren, Xiaohai He, Chuncheng Wang, and Zhibo Zhao. Adaptive consistency prior based deep network for image denoising. In *Proceedings of the IEEE/CVF conference on computer vision and pattern recognition*, pages 8596–8606, 2021.
- [40] Wenqi Ren, Jinshan Pan, Hua Zhang, Xiaochun Cao, and Ming-Hsuan Yang. Single image dehazing via multi-scale convolutional neural networks with holistic edges. *International Journal of Computer Vision*, 128:240–259, 2020.
- [41] Chitwan Saharia, Jonathan Ho, William Chan, Tim Salimans, David J Fleet, and Mhammad Norouzi. Image super-resolution via iterative refinement. *IEEE transactions on pattern analysis and machine intelligence*, 45(4):4713–4726, 2022.
- [42] Jiaming Song, Chenlin Meng, and Stefano Ermon. Denoising diffusion implicit models. *arXiv preprint arXiv:2010.02502*, 2020.
- [43] Ke Sun, Bin Xiao, Dong Liu, and Jingdong Wang. Deep high-resolution representation learning for human pose estimation. In *CVPR*, 2019.
- [44] Y. Tai, J. Yang, and X. Liu. Memnet: A persistent memory network for image restoration. In *Proceedings of the IEEE international conference on computer vision*, pages 4539–4547, 2017.
- [45] Dmitry Ulyanov, Andrea Vedaldi, and Victor Lempitsky. Deep image prior. In *Proceedings of the IEEE conference on computer vision and pattern recognition*, pages 9446–9454, 2018.
- [46] Zhendong Wang, Xiaodong Cun, Jianmin Bao, Wengang Zhou, Jianzhuang Liu, and Houqiang Li. Uformer: A general u-shaped transformer for image restoration. In *Proceedings of the IEEE/CVF conference on computer vision and pattern recognition*, pages 17683–17693, 2022.
- [47] Huan Wu, Xi Peng, Peng Hu, Mingzhi Lin, Yuliang Fu, Jie Yang, and Yizhou Yang. Clearer: Multi-scale context learning for image restoration with cross-level feature fusion. In *CVPR*, 2021.
- [48] Jinjun Xu and Stanley Osher. Iterative regularization and nonlinear inverse scale space applied to wavelet-based denoising. *IEEE Transactions on Image Processing*, 16(2):534–544, 2007.
- [49] Jun Xu, Lei Zhang, David Zhang, and Xiangchu Feng. Multi-channel weighted nuclear norm minimization for real color image denoising. In *Proceedings of the IEEE international conference on computer vision*, pages 1096–1104, 2017.
- [50] Jun Xu, Lei Zhang, and David Zhang. A trilateral weighted sparse coding scheme for real-world image denoising. In *Proceedings of the European conference on computer vision (ECCV)*, pages 20–36, 2018.
- [51] Yinglong Xu, Xiaoming Liu, and Guosheng Sun. Learning in the dct domain for fast image super-resolution. *Pattern Recognition*, 107:107466, 2020.
- [52] W. Yang and J. Sun. Bm3d-net: A convolutional neural network for image denoising inspired by bm3d algorithm. *arXiv preprint arXiv:1804.00348*, 2018.

- [53] Yang Yang and Stefano Soatto. Fda: Fourier domain adaptation for semantic segmentation. In *CVPR*, 2020.
- [54] Syed Waqas Zamir, Aditya Arora, Salman Khan, Munawar Hayat, Fahad Shahbaz Khan, and Ming-Hsuan Yang. Restormer: Efficient transformer for high-resolution image restoration. In *Proceedings of the IEEE/CVF conference on computer vision and pattern recognition*, pages 5728–5739, 2022.
- [55] Hang Zhang, Kristin Dana, Jianming Shi, Zhongyue Zhang, Xiting Wang, Anurag Tyagi, and Anurag Agrawal. Panet: Few-shot image recognition via feature pyramid aggregation. In *CVPR*, 2019.
- [56] K. Zhang, W. Zuo, Y. Chen, D. Meng, and L. Zhang. Beyond a gaussian denoiser: Residual learning of deep cnn for image denoising. *IEEE Transactions on Image Processing*, 26(7):3142–3155, 2017.
- [57] K. Zhang, W. Zuo, and L. Zhang. Ffdnet: Toward a fast and flexible solution for cnn-based image denoising. *IEEE Transactions on Image Processing*, 27(9):4608–4622, 2018.
- [58] L. Zhang, W. Zuo, and S. Gu. Poisson-gaussian noise modeling and fitting for single-image raw-data. *IEEE Transactions on Image Processing*, 28(12):6027–6040, 2019.
- [59] Dihan Zheng, Sia Huat Tan, Xiaowen Zhang, Zuoqiang Shi, Kaisheng Ma, and Chenglong Bao. An unsupervised deep learning approach for real-world image denoising. In *International Conference on Learning Representations*, 2020.
- [60] Dihan Zheng, Xiaowen Zhang, Kaisheng Ma, and Chenglong Bao. Learn from unpaired data for image restoration: A variational bayes approach. *IEEE Transactions on Pattern Analysis and Machine Intelligence*, 45(5):5889–5903, 2022.
- [61] Yuqian Zhou, Jianbo Jiao, Haibin Huang, Yang Wang, Jue Wang, Honghui Shi, and Thomas Huang. When awgn-based denoiser meets real noises. In *Proceedings of the AAAI Conference on Artificial Intelligence*, volume 34, pages 13074–13081, 2020.
- [62] Z. Zhou, M.M.R. Siddiquee, N. Tajbakhsh, J. Liang, C. Zhang, Y. Liu, Y. Yang, H. Jiang, J. Shin, J.G. Dy, et al. W2s: A dataset for weakly-supervised semantic segmentation of microscopic images with different imaging modalities. *arXiv preprint arXiv:2004.08331*, 2020.
- [63] D. Zoran and Y. Weiss. Learning image prior with a gaussian mixture model: applications to denoising. *IEEE Transactions on Image Processing*, 20(1):106–119, 2011.